RSC Advances

PAPER

View Article Online
View Journal | View Issue

Cite this: *RSC Adv.*, 2022, **12**, 28586

Decorated reduced graphene oxide transfer sulfides into sulfur and sulfone in wastewater †

Zheng Wang, [ab] Hongtao Cui, [a] Hengduo Xu[b] and Yanqing Sheng*[b]

Sulfides cannot be completely removed using oxidation due to the production of sulfate. In this work, a reduced graphene oxide (RGO)/Fe_3O_4 hybrid material was synthesized *via* a simple *in situ* chemical method for sulfide removal. The adsorption capacity of RGO/Fe_3O_4 was evaluated by sulfide removal from aqueous solution, and different experimental parameters including contact time, solution pH, adsorbent dosage, ion strength and temperature were investigated. The equilibrium data were in accordance with the Langmuir linear isotherm with a maximum uptake capacity of 173 mg g^{-1}. The adsorption of sulfide by the RGO/Fe_3O_4 hybrid material can be attributed to the synergistic effect of both chemical and physical adsorption according to kinetic, adsorption isotherm and thermodynamic studies. The RGO/Fe_3O_4 material with oxygenated functional groups could convert sulfides to stable elemental sulfur and sulfone organics. The external magnetic field could easily separate the magnetic RGO/Fe_3O_4 adsorbent from the liquid. This research provides a novel strategy for the green and low-cost treatment of sulfide-containing wastewater by the RGO/Fe_3O_4 hybrid material.

Received 13th July 2022
Accepted 21st September 2022

DOI: 10.1039/d2ra04323h

rsc.li/rsc-advances

1. Introduction

Sulfides (H_2S, HS^-, S^{2-}) are regarded as one of the most widely existing pollutants in the environment.[1] Sulfides in wastewater can react with metals and metal oxides to form metal sulfides, which can corrode metal equipment and metal pipes.[2] Sewage leakage induced by pipeline corrosion pollutes the surrounding water, soil and groundwater environment and the corrosion product iron sulfide (FeS) then causes the water body to become black, which worsens the water quality.[3] Furthermore, hydrogen sulfide (H_2S) gas released from wastewater even at trace levels can cause the water to become obnoxious and is toxic for the human nervous system.[4]

Sulfides enter the aqueous environment through both natural processes and human activities. Sulfides can be formed spontaneously by the anaerobic decomposition of sulfur-containing organic matter or the reduction of biological sulfates under the action of septic bacteria and sulfate-reducing bacteria, which usually occurs in natural systems such as marine, river and lake sediments as well as in the treatment of municipal and agricultural sewage and waste.[5] Moreover, the majority of manufactured dissolved sulfide and gaseous H_2S pollutants are discharged into the natural environment. The average sulfide concentrations in wastewater from the petrochemical and leather industries are around 150 g L^{-1} and 360 mg L^{-1}, respectively.[6,7] Dissolved sulfides also have been frequently detected in the municipal wastewater treatment, pulp and paper production, and the manufacturing of coke and steel.[1] The removal of sulfides from aqueous solutions is usually done by chemical precipitation, which is defined as sulfides reacting with metal ions such as iron and zinc ions to form insoluble precipitates.[8] However, this technology requires a large amount of precipitant input and the precipitate produced is too small to be separated; hence, the comprehensive economic benefits are not good.

Recent studies demonstrated that oxidation and adsorption have been generally adopted for sulfide removal.[9] It is well known that sulfides in wastewater mostly exist as reductive S^{2-}, which can be oxidized to elemental sulfur/sulfate by different oxidants such as air, ozone, chlorine, potassium permanganate and hydrogen peroxide.[10] However, sulfates are reduced into sulfides again by sulfate-reducing bacteria (SRB), and cannot be completely removed in many aquatic systems.[11] Adsorption is a powerful approach that has been widely used for sulfide removal due to its low cost and capability for complete removal.[12] To date, various adsorbents (including activated carbon, metal oxides, porous graphitic carbon composite and graphene-based materials) have been employed for sulfide removal. Hariz *et al.* found that activated carbon calcined at 500 °C could effectively adsorb sulfide in refining wastewater, and its adsorption capacity was 58.82 mg g^{-1}.[13] Jacukowicz-Sobala *et al.* used hybrid polymers containing iron oxides prepared through a carboxyl cation exchanger to remove

[a]*School of Chemistry and Chemical Engineering, Yantai University, Yantai 264005, China*

[b]*Key Laboratory of Coastal Zone Environmental Processes, Yantai Institute of Coastal Zone Research, Chinese Academy of Sciences, Yantai 264003, China. E-mail: yqsheng@yic.ac.cn; Tel: +86-0535-2109265*

† Electronic supplementary information (ESI) available. See https://doi.org/10.1039/d2ra04323h

sulfides from water with an adsorption capacity of 60 mg g^{-1}.[14] The sulfide was removed by heterogeneous oxidation and reductive dissolution of iron(III) oxides. Edathil *et al.* synthesized a graphene-based hybrid adsorbent using desert sand and sucrose, and the maximum adsorption capacity for sulfide was 370 mg g^{-1}.[15] The adsorption behavior of sulfide on the adsorbent fitted the Langmuir adsorption isotherm and pseudo-second-order kinetic model well. Sulfide is removed by conversion to elemental sulfur and sulfate.

Among these materials, carbon-based adsorbents have won significant consideration owing to its large specific surface area, abundant adsorption sites and good chemical stability.[16,17] In particular, reduced graphene oxide (RGO) exhibits good absorption property.[18] RGO hydrogel and aerogels had been used for the removal of toluene, rhodamine 6G and phenol with adsorption capacities of 500 mg g^{-1}, 500 mg g^{-1} and 150 mg g^{-1}, respectively, and could be reused at least five times.[19] Porous 3D RGO showed good adsorption performance for imitated polystyrene microplastics by the strong π–π interaction.[20] Moreover, RGO has been also demonstrated to have good catalytic activity in oxidative desulfurization reactions to remove sulfur-containing compounds.[21] Therefore, RGO potentially can be used as both adsorbent and catalyst to remove dissolved sulfides from waters through adsorbing and catalytically oxidizing sulfides into stable sulfur-containing organics in cases involving the secondary conversion of sulfates.

However, direct separation of RGO from solution by centrifugation or filtration is a high-cost process after adsorption, which limits its practical application. In addition, the easy aggregation of RGO will reduce the adsorption capacity.[22] These problems can be solved well by combining magnetic particles with RGO. Fe_3O_4 is the most commonly used magnetic particle, which is superparamagnetic and environmentally friendly. Furthermore, it has a large surface area and is a low-cost material.[23] RGO loaded with Fe_3O_4 can prevent the aggregation of RGO platelets, which increases the surface area and improves the adsorption capacity. Simultaneously, the magnetic adsorbent can be easily separated from the solution by an external magnetic field.

In the present study, a reduced graphene oxide/magnetite (RGO/Fe_3O_4) hybrid material was synthesized by a simple *in situ* chemical synthesis method. RGO/Fe_3O_4 was tested to remove sulfide from aqueous solution under different experimental parameters, including contact time, solution pH, adsorbent dosage, ionic strength and temperature. The hybrid material was also characterized by SEM, XRD, FTIR, XPS and BET techniques. Adsorption kinetics, isotherm models and thermodynamics were applied to determine the rate control step, maximum adsorption capacity and adsorption mechanism. Moreover, a corresponding reaction mechanism for the removal of sulfides using the RGO/Fe_3O_4 hybrid material was put forward.

2. Experimental

2.1 Materials preparation

Graphite powder (99.95%, ≥325 mesh) was purchased from Beijing InnoChem Technology (China). Other reagents and chemicals, including sodium sulfide ($Na_2S\cdot 9H_2O$), iron(II) chloride tetrahydrate ($FeCl_2\cdot 4H_2O$), sodium nitrate ($NaNO_3$), potassium permanganate ($KMnO_4$), hydrogen peroxide (H_2O_2), sulfuric acid (H_2SO_4, 98%) and hydrochloric acid (HCl, 37%), were obtained from Sinopharm Chemical Reagent (China). All chemicals were of analytically pure grade. Ultrapure water (>18 MΩ cm) was used in all experiments.

2.2 Preparation of the RGO/Fe_3O_4 hybrid material

The modified Hummers' method[24] was used to prepare graphene oxide (GO) from graphite powder (see Text S1†). Synthesis of the RGO/Fe_3O_4 hybrid material with different weight ratios of GO and $FeCl_2\cdot 4H_2O$ was carried out *via* a simple *in situ* chemical synthesis method[25] with some modifications. In a typical synthesis of the RGO/Fe_3O_4 hybrid material, GO (25 mg) was dispersed into ultrapure water (50 mL) by ultrasonication for 45 min. Then, $FeCl_2\cdot 4H_2O$ (2.0281 g) was added to this suspension under nitrogen protection. Sequentially, the mixture was stirred at ambient temperature, and 25% ammonia solution (15 mL) was mixed slowly. Each drop of ammonia solution quickly turned the solution from brown to black, and the stirring of the black mixture was maintained for 15 min. Finally, the resulting mixture was washed repeatedly with ultrapure water and ethanol to obtain a solid sample. The solid sample was freeze-dried to yield the RGO/Fe_3O_4 hybrid material. The weight ratios of GO and $FeCl_2\cdot 4H_2O$ were set to 1 : 1–1 : 4 (GO, 25 mg; $FeCl_2\cdot 4H_2O$, 1.0141, 2.0281, 3.0422, and 4.0562 g), where the obtained composites were denoted as RGO/Fe_3O_4-1, RGO/Fe_3O_4-2, RGO/Fe_3O_4-3, RGO/Fe_3O_4-4, respectively.

2.3 General characterization

The crystal structures of various composites were determined by X-ray diffraction (XRD) with the X-ray source of the Cu-Kα radiation (Ultima IV, Japan) in the range of 10–80° (2 theta). The surface morphology analysis was carried out by scanning electron microscopy (SEM) (S-4800, Hitachi, Japan). The surface functional groups of the immobilization materials were identified *via* Fourier-transform infrared spectroscopy (FTIR) (Nicolet iS50, Thermo Fisher, USA). The elemental content and chemical state of various compounds were measured by X-ray photoelectron spectroscopy (XPS) (Thermo ESCALAB 250XI, USA) with an Al Kα X-ray as the excitation source. The specific surface area was determined by the Brunauer–Emmett–Teller (BET) method (ASAP2460, Micromeritics, USA).

2.4 Chemical analysis

Various concentrations of sulfide solution were obtained by diluting the stock solution, which was prepared by dissolving 7.5 g of sodium sulfide with a small amount of water and transferring to a 1000 mL volumetric flask for diluting to line. The concentrations of sulfide before and after adsorption were determined by methylene blue method (See Text S2†). All adsorption experiments were carried out without nitrogen gas protection to mimic the actual wastewater scene.

Batch adsorption experiments were carried out by mixing a specific quantity of RGO/Fe_3O_4 in 10 mL of determined concentrations of sulfide solution, which was held in different 50 mL stoppered conical flasks. The flasks were placed in a constant temperature oscillator (ZD-85, Yinggong, China), which was kept at room temperature with a fixed speed of 160 rpm for all subsequent experiments. The main experimental parameters for the effect of adsorption, including contact time (0–180 min), pH value (2.0–12.0), adsorbent dosage (0–50.0 mg), initial sulfide concentration (0–350 mg L^{-1}) and temperature (25–45 °C). In addition, this paper explored the effect of ionic strength on sulfide adsorption, which was conducted by changing the concentrations of NaCl and $CaCl_2$ (0–1 M). The detailed experimental procedures are supplied in Text S3.† A volume (1.0 mL) of the dispersion solution was pipetted at the specified moment and filtered quickly with a 0.45 μm filter membrane. Then, the equilibrium concentrations of sulfide were quantified by UV-vis absorbance at 665 nm. All tests were repeated multiple times. The removal rate (%) and uptake capacity (Q_e, mg g^{-1}) for sulfide under equilibrium condition of the RGO/Fe_3O_4 composite were determined from eqn (1) and (2), respectively.

$$\text{Removal}\% = \left(\frac{C_0 - C_e}{C_0}\right) \times 100 \quad (1)$$

$$Q_e = \frac{V}{m}(C_0 - C_e) \quad (2)$$

where C_0 (mg L^{-1}) is the initial concentration of the sulfide solution, C_e (mg L^{-1}) is the equilibrium concentration after adsorption, V (L) is the volume of the sulfide solution, and m (g) is the weight of the adsorbent added.

For kinetic studies, linear pseudo first order, linear pseudo second order and intra-particle diffusion models were used to understand the adsorption mechanism. Equivalently, Langmuir and Freundlich adsorption isotherms in linear and non-linear forms were fitted by the sulfide uptake gained at different initial sulfide concentrations to determine the equilibrium adsorption capacity. Thermodynamic studies were carried out to further analyze the adsorption process.

Furthermore, in order to find an appropriate model to fit the adsorption data, the root mean squared error (RMSE) and χ^2 values were used to evaluate the linear and non-linear adsorption isotherm models, combined with the value of the correlation coefficient (R^2) from the regressive analysis. The expressions for the above error functions were calculated as follows:

$$\text{RMSE} = \sqrt{\frac{1}{n-2}\sum_{i-1}^{n}\left(Q_{exp} - Q_{cal}\right)^2} \quad (3)$$

$$\chi^2 = \sum_{i=1}^{n}\frac{\left(Q_{exp} - Q_{cal}\right)^2}{Q_{cal}} \quad (4)$$

where Q_{exp} is the adsorption capacity obtained experimentally, Q_{cal} is the adsorption capacity calculated from the isotherm, and n is the number of test elements.

3. Results and discussions

3.1 Characterization of the RGO/Fe_3O_4 hybrid material

3.1.1. Morphology and microstructure analysis. Fig. 1(a–d) shows the morphology of graphite, GO, fresh and used RGO/Fe_3O_4 by SEM, respectively. It can be seen that flake graphite became thin paper-like graphene oxide, confirming the successful synthesis of GO using the modified Hummers' method.[26] The RGO/Fe_3O_4 hybrid materials showed a stacked sheet-like morphology with some small irregular sheets (Fig. 1(c)). One plausible explanation for this observation is that an electrostatic attraction exists between the Fe^{2+} and graphene oxide sheets with negatively charged functional groups.[27] Fe^{2+} was oxidized to Fe^{3+} by the hydroxyl (OH), alkoxy (C–O–C) and carbonyl (C=O), and carboxylic acid (COOH), which were reduced simultaneously with the formation of RGO. The detailed redox reaction mechanisms are described in eqn (5)–(7).

$$2Fe^{2+} + GO \rightarrow 2Fe^{3+} + RGO \quad (5)$$

$$2Fe^{3+} + Fe^{2+} + 8OH^- \rightarrow Fe_3O_4 + 4H_2O \quad (6)$$

$$3Fe^{2+} + GO(8OH^-) \rightarrow Fe_3O_4 + 4H_2O + RGO \quad (7)$$

Compared with Fig. 1(c), the morphology variation of the RGO/Fe_3O_4 hybrid material adsorbed sulfide was not apparent (Fig. 1(d)), which demonstrated that there may be little relationship between the morphology and the adsorption.[28]

3.1.2. Crystal structure analysis. Fig. 2(a) provides the X-ray diffraction patterns of graphite, GO, fresh and used RGO/Fe_3O_4. The graphite exhibited a strong diffraction peak at 26.4° (002) with a corresponding interlayer spacing (d-spacing) of 0.3376 nm. From Fig. 2(a), it can be seen that a large peak shifted from 26.4° to 10.7° (001) for the GO with increased interlayer spacing of 0.8252 nm. This could be explained by the presence of oxygen-containing functional groups.[29] This result was consistent with the SEM results. The diffraction peaks of the RGO/Fe_3O_4 hybrid material at 2θ of 30.12°, 35.48°, 43.12°, 53.50°, 57.03° and 62.62° were indexed to the (220), (311), (400), (422), (511), and (440) planes of Fe_3O_4 (JCPDS#88-0866), respectively.[30] Moreover, a strong diffraction peak occurred at 2θ of 21.22° (002) with the interlayer spacing of 0.4184 nm for RGO,[31] which was caused by the Fe^{2+} reduction. The higher interlayer spacing demonstrated that some oxygen-containing functional groups were still retained in RGO.[32] These conclusions confirmed that RGO/Fe_3O_4 was well prepared by *in situ* chemical method. However, the XRD pattern of RGO/Fe_3O_4 showed no significant peak change after sulfide adsorption, which might be due to low sulfur content or the amorphous product.

3.1.3. Surface functional groups analysis. The surface properties and functional groups on the surface of GO, fresh and used RGO/Fe_3O_4 hybrid material were further studied by FTIR spectroscopy (Fig. 2(b)). In the FTIR spectrum of GO, the peak at 3450 cm^{-1} was assigned to the O–H stretching

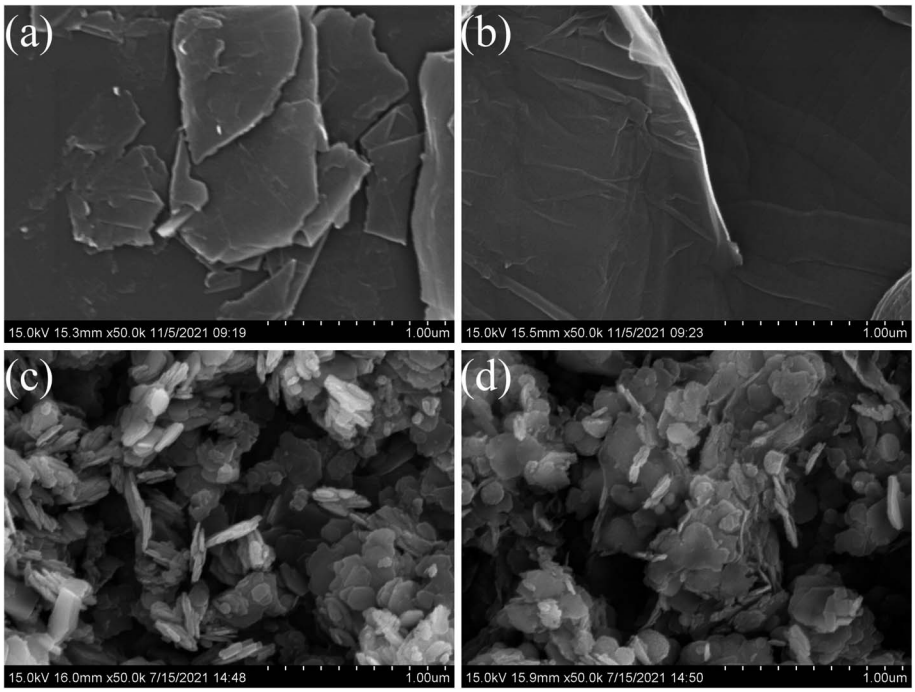

Fig. 1 SEM images of (a) graphite, (b) GO, (c) fresh RGO/Fe_3O_4 (RGO/Fe_3O_4-2) and (d) used RGO/Fe_3O_4 (RGO/Fe_3O_4-2, $C_0 = 135.88$ mg L^{-1}, $T =$ 298 K, $m = 0.050$ g, $t = 180$ min, pH = 11.74).

vibrations of water molecules that were absorbed on the samples.[33] The peak at 1720 cm^{-1} corresponded to the C=O stretching vibration of carboxyl (–COOH) groups or carbonyl (–RCO) groups,[34] and the peaks at 1290 and 1020 cm^{-1} were attributed to the C–O stretching vibration of the epoxy (C–O–C) groups.[33] The peak at 1600 cm^{-1} belonged to the C=C bond of the carbon skeleton.[33] These data indicated that GO was synthesized well. For RGO/Fe_3O_4, the above characteristic peaks of oxygen-containing functional groups were weakened, indicating that GO was partially reduced to RGO. Furthermore, the peak at 579 cm^{-1} was ascribed to the characteristic absorption band of the Fe–O bond of bulk Fe_3O_4.[35] Additionally, from the FTIR spectra of the sulfide-adsorbed RGO/Fe_3O_4, a new peak at 436 cm^{-1} was observed, which was attributed to the S–S bond,[36] indicating the formation of elemental sulfur and the adsorption of sulfides on RGO/Fe_3O_4.

3.1.4. Chemical composition analysis of fresh and used RGO/Fe_3O_4. XPS spectra were used to further determine the final form of the sulfide adsorbed on RGO/Fe_3O_4 and their interactions. Fig. S1(a) and (b)† shows the wide spectrum of fresh and used RGO/Fe_3O_4 hybrid materials, respectively. The characteristic signals of carbon (C 1s at 285 eV), iron (Fe 2p at

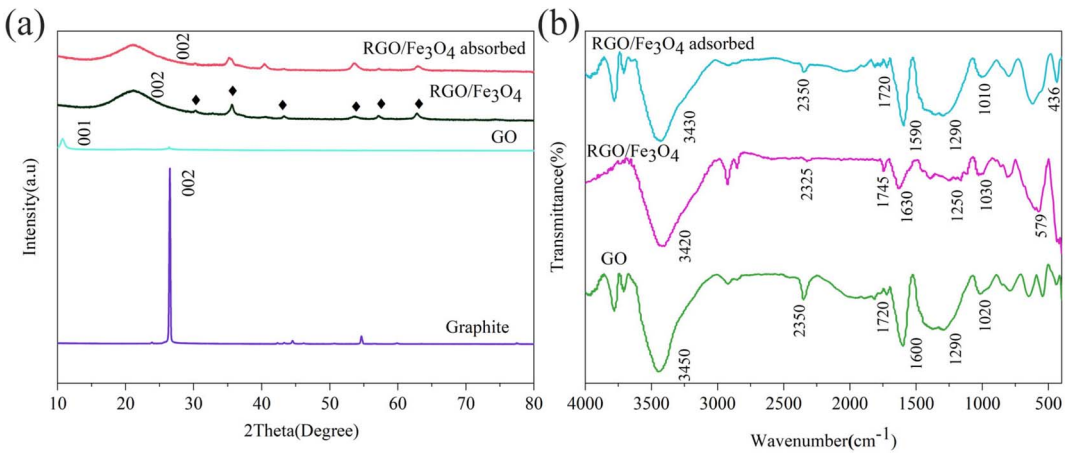

Fig. 2 XRD diffraction patterns (a) of graphite, GO, fresh and used RGO/Fe_3O_4 (RGO/Fe_3O_4-2, $C_0 = 135.88$ mg L^{-1}, $T = 298$ K, $m = 0.050$ g, $t =$ 180 min, pH = 11.74) and FTIR spectra (b) of GO, fresh and used RGO/Fe_3O_4 (RGO/Fe_3O_4-2, $C_0 = 135.88$ mg L^{-1}, $T = 298$ K, $m = 0.050$ g, $t =$ 180 min, pH = 11.74).

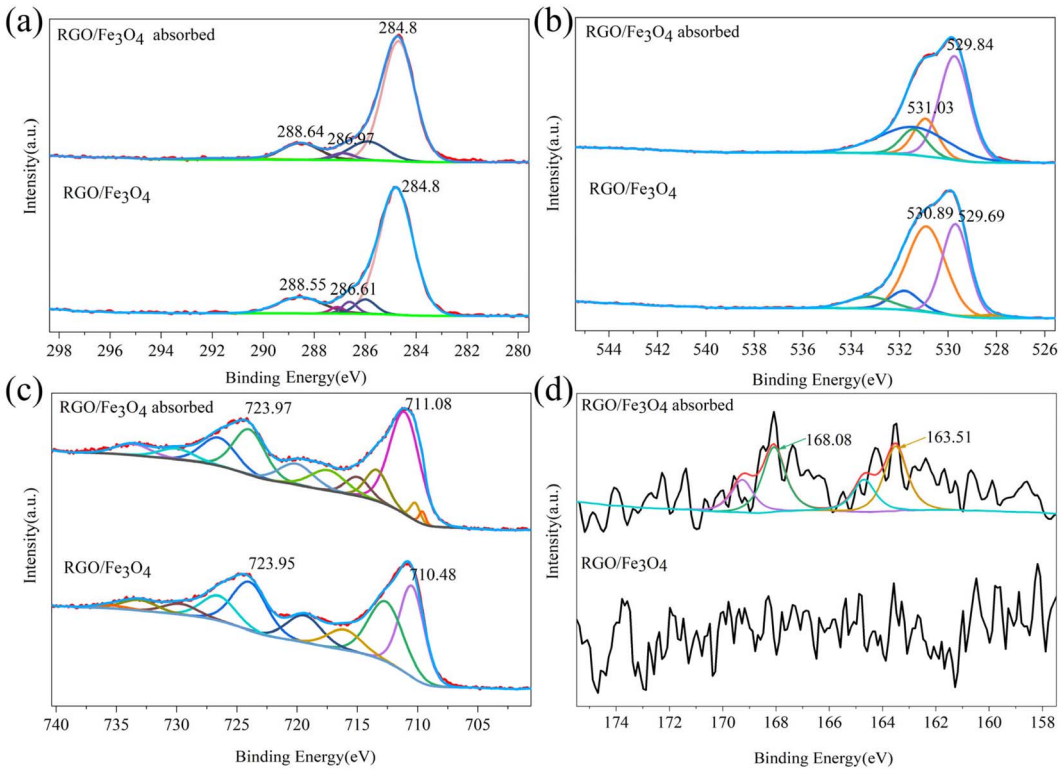

Fig. 3 XPS spectra of (a) C 1s, (b) O 1s, (c) Fe 2p and (d) S 2p of fresh and used RGO/Fe_3O_4 (RGO/Fe_3O_4-2, C_0 = 135.88 mg L^{-1}, T = 298 K, m = 0.050 g, t = 180 min, pH = 11.74).

711 eV) and oxygen (O 1s at 530 eV) were clearly observed for the fresh RGO/Fe_3O_4, which confirmed the formation of RGO/Fe_3O_4.[27] The sulfur peak was indistinct on the used RGO/Fe_3O_4 hybrid material, but the adsorption of sulfides can be determined by combining the previous results and the narrow-spectrum analysis of S 2p. The deconvoluted C 1s for RGO/Fe_3O_4 before and after the adsorption of sulfide is displayed in Fig. 3(a). The peaks of the fresh RGO/Fe_3O_4 at 284.8, 286.61 and 288.55 eV were assigned to the C–C and C=C bonding hybridization, the C–O bonds and the C=O bonds of the RGO,[37] respectively, which indicated the presence of oxygen-containing functional groups. The curve-fitted O 1s spectra of the two nanocomposites are shown in Fig. 3(b). The two characteristic peaks of the O 1s spectrum of fresh RGO/Fe_3O_4 appeared at 529.69 eV and 530.89 eV (Fig. 3(b)). The peak at 529.69 eV was associated with the lattice oxygen of Fe_3O_4,[38] while the peak at 530.89 eV indicated the existence of oxygen-containing groups like the C–O, O–C=O and O–H groups.[39] Compared to the fresh

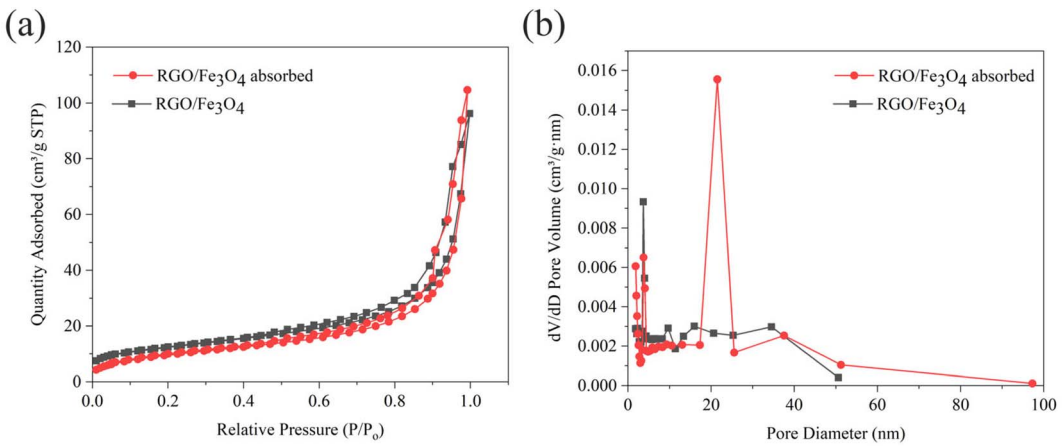

Fig. 4 (a) N_2 adsorption–desorption isotherms, and (b) pore size distribution of fresh and used RGO/Fe_3O_4 (RGO/Fe_3O_4-2, C_0 = 119.31 mg L^{-1}, T = 298 K, m = 0.4 g, t = 180 min, pH = 11.70).

Table 1 The parameters of fresh and used RGO/Fe_3O_4 (RGO/Fe_3O_4-2) obtained from BET analysis

Materials	BET surface area ($m^2\ g^{-1}$)	Average pore diameter (nm)	Total pore volume ($cm^3\ g^{-1}$)
RGO/Fe_3O_4	43.3405	13.3843	0.076190
RGO/Fe_3O_4 absorbed	35.7149	17.2854	0.161920

RGO/Fe_3O_4, the binding energies in the C 1s and O 1s spectra for the used RGO/Fe_3O_4 slightly increased. This cans be ascribed to the interaction between the sulfides and oxygen-containing groups on RGO, and their key roles in sulfide removal. As can be seen from Fig. 3(c), the Fe 2p spectrum of RGO/Fe_3O_4 showed two main peaks located at 710.48 eV and 723.95 eV, which were ascribed to the Fe $2p_{3/2}$ and Fe $2p_{1/2}$ spin–orbit peaks of Fe_3O_4, respectively.[39] The other peaks corresponded to their satellite peaks. This was similar to the result obtained from the spectra of C 1s and O 1s. The binding energies of Fe 2p also became higher in the used RGO/Fe_3O_4. This is possibly due to the strong interaction between Fe^{2+} and RGO through the Fe–O–C bonds.[40] These were in agreement with the previous XRD and FTIR characterization. Fig. 3(d) shows the S 2p spectra for the fresh and used RGO/Fe_3O_4. The S 2p spectra of fresh RGO/Fe_3O_4 had a larger peak noise and lower intensity than the used RGO/Fe_3O_4. In addition, elemental sulfur was not introduced in the material preparation process, which indicated that there were no sulfides on the fresh RGO/Fe_3O_4 composite surface. The S 2p spectra exhibited two prominent peaks at 163.51 and 168.08 eV after sulfide adsorption, corresponding to the elemental sulfur and sulfones, respectively.[41,42] These results indicated the successful adsorption and conversion of sulfides on the RGO/Fe_3O_4 composites.

3.1.5. Specific surface area and pore structure analysis of fresh and used RGO/Fe_3O_4. Fig. 4 shows the N_2 adsorption–desorption isotherms and pore size distribution of the fresh and used RGO/Fe_3O_4. The adsorption isotherms of the two samples both belong to the fourth type isotherm with H_3 hysteresis loops according to IUPCA classification,[43] which indicate that the two samples are mesoporous materials. It can be seen that the pore size distribution is mainly concentrated at about 10 nm (Fig. 4(b)). Based on the data in Table 1, the specific surface area of RGO/Fe_3O_4 was higher than that of the RGO/Fe_3O_4 absorbed. This can be explained by the fact that the oxygen-containing functional groups on the adsorbent reacted with sulfide during the adsorption process, resulting in a decrease in the amount of available oxygen functionalities, which in turn led to a decrease in the specific surface area. This phenomenon is consistent with previous research.[44] Moreover, the adsorbed sulfide will cover the surface of the material and block the micropores, which also could reduce the specific surface area.

3.2 Adsorption of sulfide

3.2.1. Adsorption effect of various RGO/Fe_3O_4 materials on sulfide. To investigate the impact of oxygen-containing functional groups on the sulfide removal efficiency and determine the optimal mass ratio of GO to $FeCl_2 \cdot 4H_2O$ for sulfide removal, four RGO/Fe_3O_4 adsorbents with a weight ratio of GO : Fe^{2+} from 1 : 1 to 1 : 4 were fabricated (denoted as RGO/Fe_3O_4-1, RGO/Fe_3O_4-2, RGO/Fe_3O_4-3, RGO/Fe_3O_4-4). As presented in Fig. 5, different initial sulfide concentrations at 19.98 mg L^{-1}, 44.60 mg L^{-1}, 83.01 mg L^{-1}, 111.55 mg L^{-1} and 134.54 mg L^{-1} were used to compare the adsorption capacity. It can be seen that the adsorption capacity of sulfide did not markedly change when the ratio of mGO and mFe^{2+} increased from 1 : 1 to 1 : 3 while fixing the initial concentrations at 19.98, 44.60, 83.01, and 111.55 mg L^{-1}, respectively. As the sulfide concentration was further increased to 134.54 mg L^{-1}, the sulfide sorption capacity of RGO/Fe_3O_4-2 (48.55 mg g^{-1}) was higher than those of RGO/Fe_3O_4-1 (48.36 mg g^{-1}), RGO/Fe_3O_4-3 (47.98 mg g^{-1}) and RGO/Fe_3O_4-4 (45.38 mg g^{-1}), respectively. Compared with the previous three compounds, the adsorption capacity of RGO/Fe_3O_4-4 slightly decreased. This is possibly because the oxygen-containing functional groups on GO were more reduced by excess Fe^{2+} during preparation of RGO/Fe_3O_4. Therefore, the sulfides cannot be fully bind to the active sites of RGO in high concentration solutions, and further resulted in a decrease in the adsorption capacity. Finally, to balance the removal efficiency and the cost, RGO/Fe_3O_4-2 was selected for further research.

3.2.2. Effect of the contact time. Inceptive adsorption tests were performed to determine the equilibrium contact time of adsorption, and the corresponding experimental results are

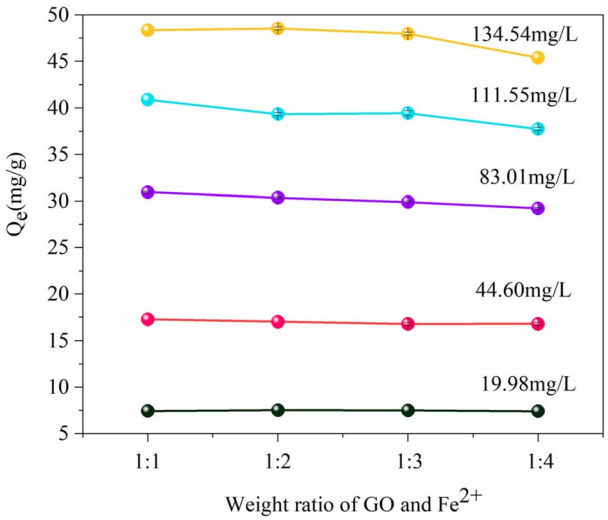

Fig. 5 The sorption capacities of various RGO/Fe_3O_4 (T = 298 K, m = 25 mg, t = 180 min). Error bars represent the standard deviation of replicate measurements.

presented in Fig. 6(a). The sulfide removal efficiency and uptake capacity increased with the contact time. It can be seen that the removal efficiency and adsorption capacity of sulfide increased rapidly in the early stage, which could be ascribed to the presence of sufficient unsaturated active sites on the fresh RGO/Fe_3O_4 composite. The effect gradually disappeared until it barely increased after 30 min. Subsequently, the adsorption processes gradually reached equilibrium at time intervals ranging from 60 to 120 min. However, upon increasing the contact time to 180 min, the removal efficiency slightly increased because the vacant sites were completely occupied, and thus the equilibrium was established. The sorption equilibrium of RGO/Fe_3O_4 for sulfide was achieved within 180 min with the adsorption capacity of 49.54 mg g^{-1}. Therefore, 180 min was determined as the contact time for subsequent experiments.

3.2.3. Effect of the initial solution pH. The impact of the initial solution pH on the removal efficiency of sulfide by RGO/Fe_3O_4 was explored at pH 1.97–11.85, and the corresponding results are shown in Fig. 6(b). The sulfide removal performance exhibited obvious fluctuations under acidic and alkaline conditions. Previous research reported that the sulfides mainly existed in the form of H_2S (aq.) and HS^- under strongly acidic conditions, while the aqueous solution predominantly contains S^{2-} along with HS^- under strongly alkaline condition.[45] When the solution pH decreased, most S^{2-} would be converted into H_2S gas, which was then dispersed from the solution into the air, decreasing the sulfide concentration and causing the low removal efficiency of sulfide according to eqn (1). However, the reaction between the adsorbent and the residual sulfide was not affected by the acidic condition. At alkaline conditions, S^{2-} remained in a relatively stable state. The obtained pH results clearly indicated that the removal of sulfide by RGO/Fe_3O_4 was not impaired, and the removal efficiency almost retained the same value. The oxygen functional groups in RGO can be classified into acidic functional groups, such as carboxyl, phenol and lactol, and basic functional groups, including ketone, quinone, and carbonyl, according to the acidic or basic nature of the aqueous solution.[32] Therefore, the adsorption removal of sulfide by RGO/Fe_3O_4 was almost unaffected by solution pH, indicating that the synthesized adsorbent could be applied to sulfur-containing wastewater at all pH values. The following batch experiments were conducted at the actual pH of the original solution.

3.2.4. Effect of the adsorbent dosage. From Fig. 6(c), we can see the effect of different doses of RGO/Fe_3O_4 hybrid materials

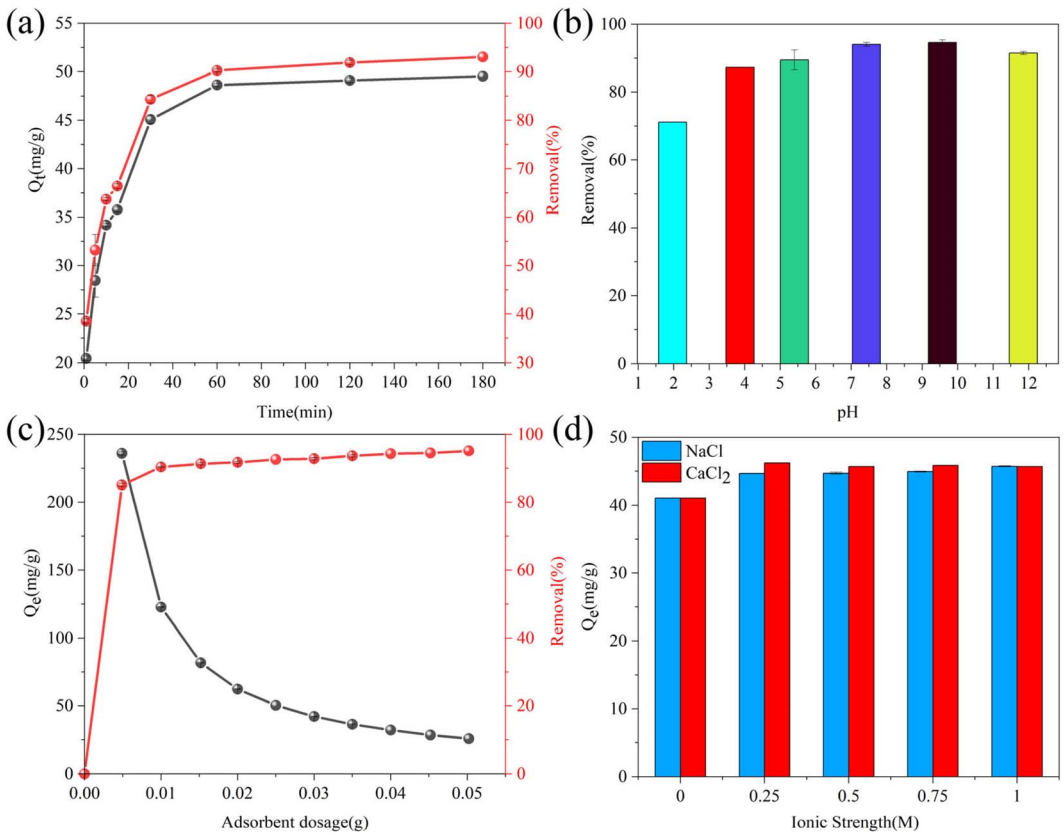

Fig. 6 (a) Effect of the contact time on sulfide adsorption using RGO/Fe_3O_4 (C_0 = 133.10 mg L^{-1}, T = 298 K, m = 25 mg, pH = 11.72). (b) Effect of pH on the sulfide removal efficiency (C_0 = 138.56 mg L^{-1}, T = 298 K, m = 25 mg, t = 180 min). (c) Effect of the adsorbent dosage on sulfide removal using RGO/Fe_3O_4 (C_0 = 135.88 mg L^{-1}, T = 298 K, t = 180 min, pH = 11.74). (d) Effect of the ionic strength on sulfide adsorption using RGO/Fe_3O_4 (C_0 = 116.72 mg L^{-1}, T = 298 K, m = 25 mg, t = 180 min, pH = 11.68). Error bars represent the standard deviation of replicate measurements.

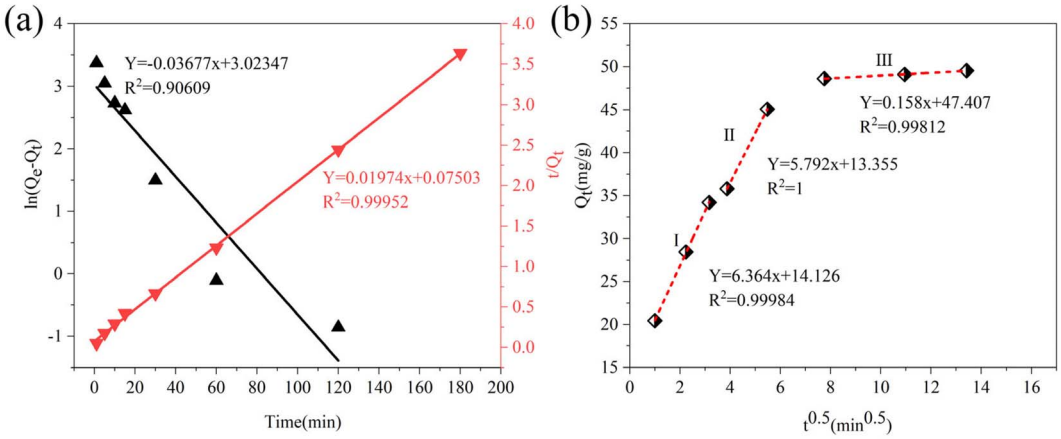

Fig. 7 Linear plots of (a) PFO and PSO models, and (b) IPD model (C_0 = 133.10 mg L^{-1}, T = 298 K, m = 25 mg, pH = 11.72).

(5–50 mg) on the sulfide removal efficiency and adsorption capacity. The results showed that the sulfide removal efficiency increased as the adsorbent dosage increased, and attained a maximum of 95.11% for 50.0 mg. This phenomenon could be explained as follows: the available active sites for adsorption increased with the increased amount of RGO/Fe_3O_4, leading to a higher adsorption capacity. Furthermore, there was a decrease in the adsorption capacity from 235.91 to 25.75 mg g^{-1} when varying the dosage of the adsorbent from 5 to 50 mg, which might be due to the increase of unsaturated adsorption sites. The increase of the adsorbent dosage with constant sulfide solution concentration will increase the amount of unsaturated active sites, which results in the decrease of sulfide content per unit mass of adsorbent, meaning a decrease in the adsorption capacity.[46] However, the removal efficiency did not change much when the adsorbent dosing was higher than 25.0 mg because of the absence of sulfide ions bound to the adsorption site. Furthermore, there might be interference between the binding sites when the amount of adsorbent was too much.[47] Therefore, considering both results and costs, the adsorbent dosage was selected as 25 mg for all of the subsequent optimization and kinetic studies.

3.2.5. Effect of the ionic strength. Because wastewater usually contains salt, it is important to investigate the effect of the ionic strength in the sulfide adsorption on RGO/Fe_3O_4. The presence of salts will compete with the sulfide species for available adsorption sites.[9] In the present study, NaCl and $CaCl_2$ were used to simulate the ionic strength on the removal of sulfide. Interestingly, the adsorption capacity of sulfide increased when increasing the NaCl and $CaCl_2$ concentrations from 0.25 to 1 M, and the growth extent of $CaCl_2$ was larger (Fig. 6(d)). Previous research reported that increasing the $CaCl_2$ (0–1.0 M) and NaCl (0–0.5 M) concentration could both decrease the adsorption capacity.[12] A possible explanation for this might be the diffuse double layer theory. The thickness of the electric double layer can be compressed by the addition of electrolyte,

Table 2 Corresponding equations and parameters of the PFO and PSO kinetic models and IPD model for sulfide adsorption on the RGO/Fe_3O_4 adsorbent

Model	Parameters	
Pseudo-first order $\ln(Q_e - Q_t) = \ln(Q_e) - k_f t$	k_f (min^{-1})	0.03677
	$Q_{e(cal)}$ (mg g^{-1})	20.56
	$Q_{e(exp)}$ (mg g^{-1})	49.54
	R^2	0.9061
Pseudo-second order $\frac{t}{Q_t} = \frac{1}{k_s Q_e^2} + \frac{t}{Q_e}$	k_s (mg^{-1} min^{-1})	0.005193
	$Q_{e(cal)}$ (mg g^{-1})	50.65
	$Q_{e(exp)}$ (mg g^{-1})	49.54
	R^2	0.9995
Intraparticle diffusion $Q_e = k_i t^{0.5} + C_i$	k_1 (mg g^{-1} $min^{-0.5}$)	6.364
	C_1	14.13
	R_1^2	0.9998
	k_2 (mg g^{-1} $min^{-0.5}$)	5.792
	C_2	13.36
	R_2^2	1.0000
	k_3 (mg g^{-1} $min^{-0.5}$)	0.1580
	C_3	47.41
	R_3^2	0.9981

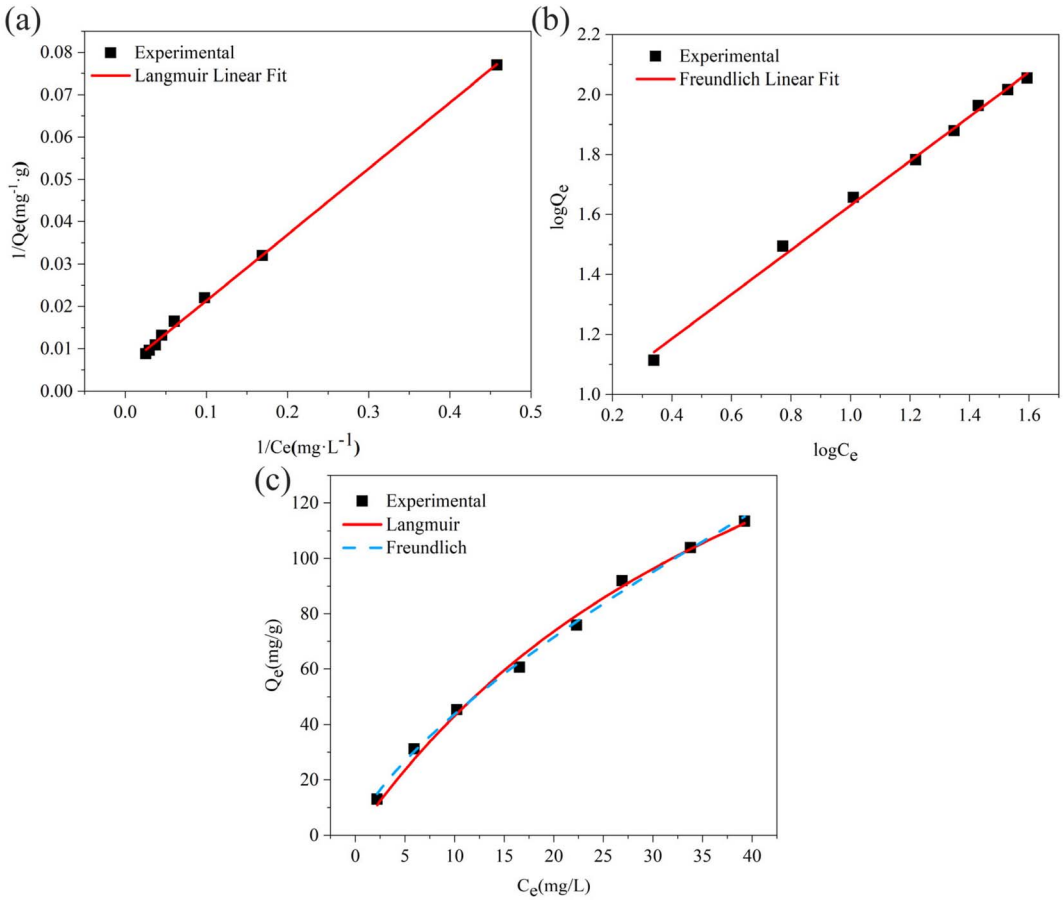

Fig. 8 (a) Linear Langmuir adsorption isotherm, (b) linear Freundlich adsorption isotherm, (c) non-linear Langmuir and Freundlich adsorption isotherms (C_0 = 34.54–325.06 mg L^{-1}, T = 298 K, m = 25 mg, t = 180 min).

which weakens the electrostatic interaction between the adsorbate and the adsorbent.[48] This inconsistency could be due to the existence of electrostatic repulsion between the RGO/Fe_3O_4 and sulfide, which would be impaired after adding KCl and $CaCl_2$. Therefore, the sulfide adsorption was further enhanced. Furthermore, it is clear that the Ca^{2+} has a more apparent effect than K^+. The reason could be that Ca^{2+} could form intramolecular bridges such as R–COO^-–Ca^{2+}–$^-$OOC–R,[49] which further screened the negative charges of the adsorbent and interfered with the electrostatic repulsion.

3.2.6. Adsorption kinetic. Adsorption kinetic analysis was used to investigate the adsorption rate and reaction mechanism of the adsorption process of sulfide by RGO/Fe_3O_4. In this work, the adsorption kinetics data were fitted using the pseudo-first-order (PFO) model, pseudo-second-order (PSO) model and intraparticle diffusion (IPD) model.[50] The corresponding linear

Table 3 Linear and nonlinear isotherm models and parameters of the Freundlich and Langmuir models for sulfide adsorption on RGO/Fe_3O_4

Model	Parameters	
Langmuir linear isotherm $\frac{1}{Q_e} = \left(\frac{1}{Q_{max} \times K_L}\right) \frac{1}{C_e} + \frac{1}{Q_{max}}$	q_{max} (mg g^{-1})	173.01
	K_L	0.0371
	R^2	0.9987
Langmuir non-linear isotherm $Q_e = \frac{q_{max} K_L C_e}{1 + K_L C_e}$	q_{max} (mg g^{-1})	251.32
	K_L	0.0207
	R^2	0.9940
Freundlich linear isotherm $\log q_e = \log K_F + \frac{1}{n} \log C_e$	$1/n$	0.7406
	K_F	7.76
	R^2	0.9960
Freundlich non-linear isotherm $Q_e = K_F C_e^{\frac{1}{n}}$	$1/n$	0.7069
	K_F	8.60
	R^2	0.9960

Table 4 RMSE and χ^2 values of the linear and nonlinear adsorption isotherm models for sulfide adsorption onto RGO/Fe_3O_4

Model		Parameters	
		RMSE	χ^2
Langmuir	Linear	0.0009	0.0004
	Non-linear	2.8998	1.3837
Freundlich	Linear	0.0217	0.0019
	Non-linear	2.1782	0.5735

Table 5 Comparison of the equilibrium time and q_{max} of sulfide by various materials

Materials	Time (min)	q_{max} (mg g^{-1})
HIX[1]	180	150.00
PGC[12]	180	149.25
MAC-500 °C (ref. 13)	30	58.82
AIg/iron oxide-NP[56]	180	136.90
GSH composites[15]	180	370.40
MnO_2-PGC[9]	180	526.32
RGO/Fe_3O_4 (this research)	180	173.01

Table 6 Thermodynamic parameters for the adsorption of sulfide on RGO/Fe_3O_4

Temperature (K)	ΔG (kJ mol^{-1})	ΔH (kJ mol^{-1})	ΔS (J mol^{-1} K^{-1})
298	−3.2732	5.762	30.4145
308	−3.6663		
318	−3.8776		

plots and parameters of the PFO and PSO models are displayed in Fig. 7(a) and Table 2, respectively. Q_e is the uptake capacity at the equilibrium of the RGO/Fe_3O_4 composite for sulfide, Q_t is the uptake capacity at time "t", k_f represents the pseudo-first-order rate constant and k_s represents the pseudo-second-order rate constant. It can be seen that the correlation coefficient R^2 obtained by the PSO model was larger than that for the PFO model, and the experimentally measured adsorption capacity ($Q_{e(exp)} = 49.54$ mg g^{-1}) was close to the theoretical value ($Q_{e(cal)} = 50.65$ mg g^{-1}). This showed that PSO model could better describe the adsorption of sulfide by RGO/Fe_3O_4. Meanwhile, this further indicated that sulfide adsorption on the RGO/Fe_3O_4 hybrid material followed a chemisorption mechanism with a rate constant of 0.005193 mg^{-1} min^{-1}.[51] This behavior was in agreement with the characterization results obtained from the used RGO/Fe_3O_4.

Fig. 7(b) shows the plot of the IPD model, and the corresponding parameter is presented in Table 2. C_i represents the boundary layer thickness and k_i represents the intra-particle diffusion constant, where "i" represents the different stages. The greater the C value, the greater the boundary layer effect.[52] As can be seen from Fig. 7(b), the adsorption of sulfide by RGO/Fe_3O_4 presents a multi-level linear relationship. At the beginning, Q_t increased rapidly with time t, then rose slowly, and finally tended to be in dynamic equilibrium, indicating that two or more diffusion steps affecting the rate control were involved in the whole adsorption process. The rapidly rising stage indicated that sulfide diffused from the solution to the outer surface of the adsorbent with a relatively high rate constant ($k_1 = 6.364$ mg g^{-1} $min^{-0.5}$). The subsequent ascending phase indicated that sulfide passed through the liquid membrane and onto the RGO/Fe_3O_4 surface with a smaller rate constant ($k_2 = 5.792$ mg g^{-1} $min^{-0.5}$). In the equilibrium stage, the rate constant decreased significantly ($k_3 = 0.158$ mg g^{-1} $min^{-0.5}$), which may be due to the reduction of adsorption sites and the electrostatic repulsion between the sulfides on RGO/Fe_3O_4 and the aqueous solution. It is obvious that none of the three lines goes through the origin, so the adsorption pathways of sulfide on RGO/Fe_3O_4 may be controlled by other processes besides intra-particle diffusion.[53]

3.2.7. Equilibrium study. To investigate the sulfide adsorption mechanism and the maximum adsorption capacity on the RGO/Fe_3O_4 hybrid material, linear and nonlinear plots of Freundlich and Langmuir adsorption isotherms were used and the corresponding parameters are shown in Fig. 8 and Table 3, respectively. K_L is the Langmuir adsorption constant, K_F is the reaction rate constant of the Freundlich linear model, and $1/n$ (dimensionless) is the affinity of adsorption. According to the R^2 of the adsorption isotherm, the Langmuir linear model can fit the experimental data better than the Freundlich linear model with the maximum uptake capacity of 173.01 mg g^{-1}, which indicated that the adsorption of sulfide by RGO/Fe_3O_4 was a monolayer adsorption. The Freundlich linear isotherm assumed that the adsorption was multilayer and occurred on heterogeneous surfaces. The value of $1/n$ (0.7406) obtained from the Freundlich linear equation was between 0.1 and 1.0, which indicated that this isotherm was also favorable to describe the adsorption of sulfide on RGO/Fe_3O_4.[54]

To accurately represent the equilibrium data, Langmuir and Freundlich non-linear sorption isotherms were also adopted and are shown in Fig. 8(c). The data revealed that the equilibrium data were well fitted to the Freundlich model with a higher R^2 when compared to the Langmuir non-linear isotherm model. The obtained value of $1/n$ (0.7069) of the isotherm was fine $\left(0 < \frac{1}{n} < 1\right)$. For the Langmuir non-linear isotherm, R^2 (0.9940) was lower than the value obtained from the Langmuir linear equation (0.9987), but q_{max} (251.32 mg g^{-1}) was higher.

R^2, RMSE and χ^2 values were used to determine the most suitable adsorption isotherm model.[55] As observed from Table 4, the RMSE and χ^2 values of the Langmuir linear isotherm model were lower than those of the Freundlich linear isotherm model and the other two non-linear isotherm models, which revealed that the Langmuir linear model was the best fitting isotherm. Therefore, the adsorption process of sulfide on RGO/Fe_3O_4 was monolayer and the maximum adsorption capacity estimated was 173.01 mg g^{-1}, which was relatively higher than the values for other sulfide adsorbents presented in the literature (Table 5). Consequently, RGO/Fe_3O_4 could be used as an effective adsorbent for sulfide.

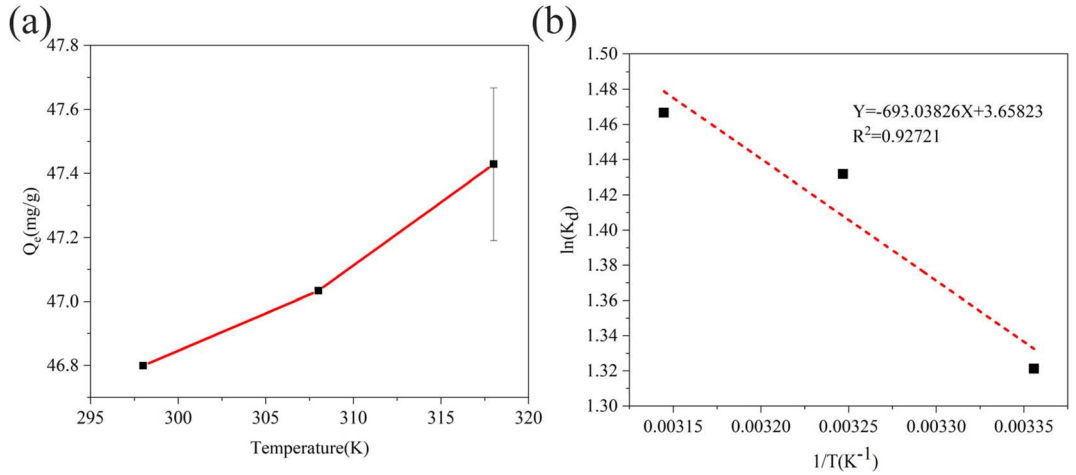

Fig. 9 (a) Effect of temperature on sulfide adsorption using RGO/Fe_3O_4 (C_0 = 130.23 mg L^{-1}, m = 25 mg, t = 180 min, pH = 11.72). Error bars represent the standard deviation of replicate measurements. (b) The plot of ln(K_d) *vs.* 1/T for the sulfide adsorption on RGO/Fe_3O_4.

3.2.8. Thermodynamic study. It is not sufficient to determine the adsorption of sulfide on RGO/Fe_3O_4 as chemisorption by adsorption kinetics. A thermodynamic study is a good complement to further investigate the adsorption process. Fig. 9(a) shows the effect of temperature on the adsorption of sulfide by RGO/Fe_3O_4. It can be seen from the figure that the adsorption capacity increased with the increase of temperature, which indicated the endothermic nature of the adsorption process. Three thermodynamic parameters, ΔG (Gibbs free energy of adsorption), ΔH (enthalpy change), and ΔS (entropy change) were employed to better understand the adsorption process, which can be obtained through eqn (8)–(10), respectively:[57]

$$K_d = \frac{q_e}{C_e} \tag{8}$$

$$\Delta G = -RT \ln K_d \tag{9}$$

$$\ln K_d = \frac{\Delta S}{R} - \frac{\Delta H}{RT} \tag{10}$$

where, K_d (L g^{-1}) is the equilibrium constant value, q_e (mg g^{-1}) is the equilibrium concentration of sulfide on RGO/Fe_3O_4, C_e (mg L^{-1}) is the equilibrium concentration, R is the gas constant, R = 8.314 J mol^{-1} K^{-1}, and T (K) is the system temperature. ΔS (J mol^{-1} K^{-1}) and ΔH (kJ mol^{-1}) are obtained from the linear plot of ln K_d *versus* 1/T.

Fig. 9(b) shows the Van't Hoff plot for sulfide adsorption on RGO/Fe_3O_4 (eqn. (10)). The thermodynamic parameters of RGO/Fe_3O_4 adsorption of sulfide are presented in Table 6. The negative ΔG at all temperatures indicates that the adsorption of sulfide by RGO/Fe_3O_4 is spontaneous. A positive value of ΔH indicates an endothermic adsorption process. ΔS is positive, revealing that the thermodynamic disorder increases during the adsorption of sulfide on RGO/Fe_3O_4. In addition, the values calculated for the Gibbs free energy of adsorption were −3.2732,

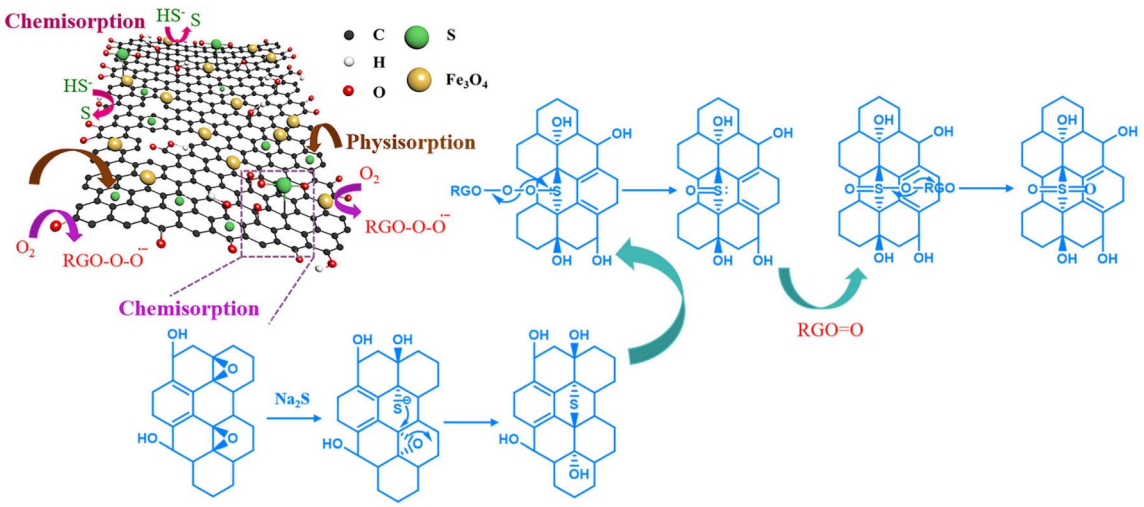

Fig. 10 Potential mechanism of sulfide removal by the RGO/Fe_3O_4 hybrid material.

−3.6663 and −3.8776 kJ mol^{-1} at 298 K, 308 K and 318 K, respectively, which was beyond the range of −80 to −400 kJ mol^{-1}, so the adsorption of sulfide by RGO/Fe_3O_4 is a physical process.[58]

3.3 Reaction mechanism

Based on the kinetics, adsorption isotherm and thermodynamic studies, the adsorption of sulfide by the RGO/Fe_3O_4 hybrid material can be attributed to the synergistic effect from both chemical and physical adsorption.[59] According to the analysis of the material characterization and adsorption experiments, the potential mechanism of sulfide removal by the RGO/Fe_3O_4 hybrid material is proposed and shown in Fig. 10. Sodium sulfide ($Na_2S \cdot 9H_2O$) exists in solution as S^{2-}, HS^-, and H_2S. On the one hand, sulfide can enter the adsorbent channel easily due to the large average pore diameter of RGO/Fe_3O_4 (13.3843 nm). The absolute values of ΔH (5.762 KJ mol^{-1}) obtained from the thermodynamic study is in the range of 4–10 kJ mol^{-1}, which indicated that sulfide could be removed through physical adsorption, such as van der Waals force.[60] On the other hand, when these compounds contacted with the RGO/Fe_3O_4 composites, sulfides transferred into elemental sulfur by reacting with hydroxyl (−OH) and carboxyl (−COOH) groups on the RGO/Fe_3O_4 surface.[61] Furthermore, epoxy (C–O–C) groups on RGO reacted with S^{2-} and formed thiols. These thiols then underwent a regioselective epoxy ring-opening dimerization reaction with the adjacent epoxy groups to generate thioethers again because the above reactions could proceed smoothly at room temperature.[62] On the other hand, the electronic structures of the contiguous carbon atoms on the RGO surfaces were altered by the carbonyl (C=O) groups, which further facilitated the adsorption and activation of dissolved oxygen in water.[63] Then, the actively adsorbed oxygen was transformed to O_2^- radicals (RGO–$OO^{\bullet -}$),[21] and the oxygen from RGO–$OO^{\bullet -}$ could be caught by the sulfur atom of thioethers with two lone pair electrons. Then, the O–O bond broke up to form both RGO=O and sulfoxide. Subsequently, the sulfoxide was rapidly oxidized to sulfone because sulfoxide cannot be stable in the presence of the highly active species RGO=O.[64] Lastly, the active sites were gained for next adsorption and activation.[21] In addition, the quantitative analysis of elemental sulfur and sulfone accumulated on the RGO/Fe_3O_4 surface and sulfur compounds in the solution after adsorption need to be further carried out to define the species and content of the products completely.

4. Conclusion

In this study, a RGO/Fe_3O_4 adsorbent was synthesized by an *in situ* chemical method, which was used to remove sulfide from aqueous solution. The adsorption process consists of chemical adsorption and physical adsorption. Through adsorption and oxidation processes, the sulfide was converted into stable elemental sulfur and sulfone, and the secondary conversion of sulfates was thus avoided. The sulfide adsorption by RGO/Fe_3O_4 reached equilibrium within a contact time of 180 min in a wide pH range. Na^+ and Ca^{2+} improved the sulfide sorption capacity of RGO/Fe_3O_4 because of the weak electrostatic repulsion. The sulfide adsorption was well fitted to the pseudo-second-order kinetic model. The Langmuir linear isotherm gave a better fit, and the maximum monolayer Langmuir adsorption capacity was estimated to be 173.01 mg g^{-1}. Our thermodynamic study revealed that the adsorption of sulfide by RGO/Fe_3O_4 was a spontaneous endothermic process. In summary, the RGO/Fe_3O_4 hybrid material can serve as a potential adsorbent that offers new insight into the treatment of sulfide-containing wastewater.

Conflicts of interest

There are no conflicts to declare.

Acknowledgements

This work was supported by the Key Project of Shandong Provincial Natural Science Foundation (Grant No. ZR2020KE048) and the Strategic Priority Research Program of the Chinese Academy of Sciences (Grant No. XDA23050203).

References:

1 Ł. J. Wilk, A. Ciechanowska and E. Kociołek-Balawejder, *Sep. Purif. Technol.*, 2020, **231**, 115882.
2 F. Shi, L. Zhang, J. Yang, M. Lu, J. Ding and H. Li, *Corros. Sci.*, 2016, **102**, 103–113.
3 J. Cao, Q. Sun, D. Zhao, M. Xue, Q. Shen, D. Wang, Y. Wang and S. Ding, *J. Hazard. Mater.*, 2020, **385**, 121511.
4 J. Zhang, Q. Zhu and Z. Xing, *J. Hazard. Mater.*, 2020, **390**, 122049.
5 Ł. J. Wilk, A. Ciechanowska and E. Kociołek-Balawejder, *Materials*, 2020, **13**, 1–19.
6 M. Wiemann, H. Schenk and W. Hegemann, *Water Res.*, 1998, **32**, 774–780.
7 D. Andreides, Z. Varga, D. Pokorna and J. Zabranska, *J. Water Process. Eng.*, 2021, **40**, 101834.
8 L. Altaş and H. Büyükgüngör, *J. Hazard. Mater.*, 2008, **153**, 462–469.
9 P. K. Anjali Achazhiyath Edathil and F. Banat, *Environ. Pollut.*, 2020, **266**, 115218.
10 L. Zhang, P. D. Schryver, B. D. Gusseme, W. D. Muynck, N. Boon and W. Verstraete, *Water Res.*, 2008, **42**, 1–12.
11 J. Sun, L. Wei, R. Yin, F. Jiang and C. Shang, *Water Res.*, 2020, **171**, 115453.
12 A. A. Edathil, P. Pal and F. Banat, *J. Environ. Chem. Eng.*, 2017, **5**, 1998–2009.
13 I. B. Hariz and L. Monser, *Water Sci. Technol.*, 2014, **4**, 264–267.
14 I. Jacukowicz-Sobala, L. J. Wilk, K. Drabent and E. Kociolek-Balawejder, *J. Colloid Interface Sci.*, 2015, **460**, 154–163.
15 A. A. Edathil, J. H. Zain, M. A. Haija and F. Banat, *New J. Chem.*, 2019, **43**, 3500–3512.
16 Y. Pan, M. Chen, M. Hu, M. Tian, Y. Zhang and D. Long, *Appl. Catal., B*, 2020, **262**, 118266.
17 J. H. Yang, *Korean J. Chem. Eng.*, 2021, **38**, 674–691.

18 M. Khaleghi Abbasabadi, A. Rashidi, J. Safaei-Ghomi, S. Khodabakhshi and R. Rahighi, *J. Sulfur Chem.*, 2015, **36**, 660–671.
19 R. Castaldo, R. Avolio, M. Cocca, M. E. Errico, M. Lavorgna, J. Šalplachta, C. Santillo and G. Gentile, *Chem. Eng. J.*, 2022, **430**, 133162.
20 F. Yuan, L. Yue, H. Zhao and H. Wu, *Water Sci. Technol.*, 2020, **81**, 2163–2175.
21 Q. Gu, G. Wen, Y. Ding, K.-H. Wu, C. Chen and D. Su, *Green Chem.*, 2017, **19**, 1175–1181.
22 P. Benjwal, M. Kumar, P. Chamoli and K. K. Kar, *RSC Adv.*, 2015, **5**, 73249–73260.
23 P. Mandal and A. P. Chattopadhyay, *Dalton Trans.*, 2015, **44**, 11444–11456.
24 W. Zhang, X. Zou and J. Zhao, *J. Mater. Chem. C*, 2015, **3**, 2788–2791.
25 Z. Feng, C. Zhang, J. Chen, Y. Wang, X. Jin, R. Zhang and J. Hu, *RSC Adv.*, 2013, **3**, 4408–4415.
26 X. Zou, Y. Zhou, S. Chen, W. Li, Y. Qiang, B. Xiang, Q. Wu, F. Chen and W. Huang, *J. Alloys Compd.*, 2019, **782**, 17–27.
27 G. Bharath, R. Madhu, S.-M. Chen, V. Veeramani, D. Mangalaraj and N. Ponpandian, *J. Mater. Chem. A*, 2015, **3**, 15529–15539.
28 N. Wang, J. Feng, J. Chen, J. Wang and W. Yan, *Chem. Eng. J.*, 2017, **316**, 33–40.
29 K. Krishnamoorthy, M. Veerapandian, K. Yun and S. J. Kim, *Carbon*, 2013, **53**, 38–49.
30 J. Xu, H. Yang, W. Fu, K. Du, Y. Sui, J. Chen, Y. Zeng, M. Li and G. Zou, *J. Magn. Magn. Mater.*, 2007, **309**, 307–311.
31 M. H. Kahsay, N. Belachew, A. Tadesse and K. Basavaiah, *RSC Adv.*, 2020, **10**, 34916–34927.
32 Y. J. Oh, J. J. Yoo, Y. I. Kim, J. K. Yoon, H. N. Yoon, J.-H. Kim and S. B. Park, *Electrochim. Acta*, 2014, **116**, 118–128.
33 J. Wu, Z. Ye, W. Liu, Z. Liu and J. Chen, *Ceram. Int.*, 2017, **43**, 13146–13153.
34 L. Zhou, H. Deng, J. Wan, J. Shi and T. Su, *Appl. Surf. Sci.*, 2013, **283**, 1024–1031.
35 C.-L. Lin, C.-F. Lee and W.-Y. Chiu, *J. Colloid Interface Sci.*, 2005, **291**, 411–420.
36 T. Heitmann and C. Blodau, *Chem. Geol.*, 2006, **235**, 12–20.
37 X. Zhao, Y. Jia and Z. H. Liu, *J. Colloid Interface Sci.*, 2019, **536**, 463–473.
38 V. Karthika, M. S. AlSalhi, S. Devanesan, A. A. Kasi Gopinath and M. Govindarajan, *Sci. Rep.*, 2020, **10**, 18912.
39 M. Pudukudy, Q. Jia, Y. Dong, Z. Yue and S. Shan, *RSC Adv.*, 2019, **9**, 32517–32534.
40 N. A. Zubir, C. Yacou, J. Motuzas, X. Zhang and J. C. D. d. Costa, *Sci. Rep.*, 2014, **4**, 4594.
41 N. R. Urban, K. Ernst and S. Bernasconi, *Geochim. Cosmochim. Acta*, 1999, **63**, 837–853.
42 R. Pietrzak, T. Grzybek and H. Wachowska, *Fuel*, 2007, **86**, 2616–2624.
43 M. Thommes, K. Kaneko, A. V. Neimark, J. P. Olivier, F. Rodriguez-Reinoso, J. Rouquerol and K. S. W. Sing, *Pure Appl. Chem.*, 2015, **87**, 1051–1069.
44 I. Kondratowicz, M. Nadolska, S. Şahin, M. Łapiński, M. Prześniak-Welenc, M. Sawczak, E. H. Yu, W. Sadowski and K. Żelechowska, *Appl. Surf. Sci.*, 2018, **440**, 651–659.
45 B.-W. Pang, C.-H. Jiang, M. Yeung, Y. Ouyang and J. Xi, *J. Hazard. Mater.*, 2017, **324**, 732–738.
46 A. A. Edathil, P. Kannan, M. A. Haija and F. Banat, *Environ. Res.*, 2021, **196**, 110429.
47 G. Chen and L. Shi, *RSC Adv.*, 2017, **7**, 43445–43454.
48 J. D. Filius, D. G. Lumsdon, J. C. L. Meeussen, T. Hiemstra and W. H. V. Riemsdijk, *Geochim. Cosmochim. Acta*, 2000, **64**, 51–60.
49 K. Vermöhlen, H. Lewandowski, H.-D. Narres and M. J. Schwuger, *Colloids Surf., A*, 2000, **163**, 45–53.
50 T. M. Berhanea, J. Levya, M. P. S. Krekelerb and N. D. Danielson, *Chemosphere*, 2017, **176**, 231–242.
51 Y.-S. Ho, *J. Hazard. Mater.*, 2006, **136**, 681–689.
52 G. McKay, M. S. Otterburn and J. A. Aga, *Water, Air, & Soil Pollution*, 1985, **24**, 307–322.
53 A. H. Jawad, N. S. A. Mubarak and A. S. Abdulhameed, *J. Polym. Environ.*, 2019, **28**, 624–637.
54 R. Han, J. Zhang, P. Han, Y. Wang, Z. Zhao and M. Tang, *Chem. Eng. J.*, 2009, **145**, 496–504.
55 A. R. P. Hidayat, D. O. Sulistiono, I. K. Murwani, B. F. Endrawati, H. Fansuri, L. L. Zulfa and R. Ediati, *J. Environ. Chem. Eng.*, 2021, **9**, 106675.
56 P. Pal, A. A. Edathil, L. Chaurasia, K. Rambabu and F. Banat, *Polym. Bull.*, 2018, **75**, 5455–5475.
57 H. V. Tran, L. T. Hoang and C. D. Huynh, *Chem. Phys.*, 2020, **535**, 110793.
58 M. Hadadian, E. K. Goharshadi, M. M. Fard and H. Ahmadzadeh, *Appl. Phys. A*, 2018, **124**, 239.
59 X.-L. Sun, Z. Liu and Z.-L. Cheng, *J. Hazard. Mater.*, 2021, **403**, 123851.
60 B. von Oepen, W. Kördel and W. Klein, *Chemosphere*, 1991, **22**, 285–304.
61 A. A. Edathil, P. Kannan, M. AbuHaija and F. Banat, *Environ. Res.*, 2021, **196**, 110429.
62 K. Tatsuta, Y. Suzuki, T. Toriumi, Y. Furuya and S. Hosokawa, *Tetrahedron Lett.*, 2007, **48**, 8018–8021.
63 X. Lu, W.-L. Yim, B. H. R. Suryanto and C. Zhao, *J. Am. Chem. Soc.*, 2015, **137**, 2901–2907.
64 S. Chen, W. Lu, Y. Yao, H. Chen and W. Chen, *React. Kinet., Mech. Catal.*, 2013, **111**, 535–547.